Temperature-Insensitive Two-Dimensional Vector Bending Sensor Based on Fabry-Pérot Interferometer Incorporating a Seven-Core Fiber

Beibei Qi , Baijin Su , Fan Zhang, Ou Xu , and Yuwen Qin

Abstract—We proposed and experimentally demonstrated a temperature-insensitive two-dimensional (2D) vector bending sensor on the basis of Fabry-Pérot Interferometer (FPI). The sensor is fabricated by splicing a section of silica capillary optical fiber (COF) between a trench-assisted seven-core fiber (SCF) and a multimode fiber (MMF). For orientation angle from $0°$ to $360°$, the vector bending responses of six outer-core FPIs were studied at a step of $30°$. From experimental results, the proposed sensor exhibits strong bending-direction dependence, and the maximum sensitivity is 200.6 pm/m^{-1}. The curvature magnitude and orientation angle can be reconstructed through the dip wavelength shifts of any two off-diagonal outer-core FPIs. Hence, there are 12 various combinations from six outer-core FPIs, and the average value can be taken in multiple reconstructions to develop exact 2D vector bending measurement. For curvature magnitude and orientation angle reconstructed, the average relative error is 6.2% and 3.3%, respectively. In addition, experiments verified the proposed sensor is insensitive to ambient temperature changes.

Index Terms—Two-dimensional (2D) vector bending, seven-core fiber (SCF), Fabry–Pérot interferometer (FPI), silica capillary optical fiber (COF).

I. INTRODUCTION

OPTICAL fiber sensors have the superiorities of corrosion resistance, anti-electromagnetic interference, high safety, integration of transmission and sensing and so on. Since the late

Beibei Qi, Baijin Su, Fan Zhang, and Ou Xu are with the Advanced Institute of Photonics Technology, School of Information Engineering, Guangdong University of Technology, Guangzhou, Guangdong 510006, China, and also with the Guangdong Provincial Key Laboratory of Information Photonics Technology, Guangdong University of Technology, Guangzhou, Guangdong 510006, China (e-mail: qibeibei20@163.com; baijinsu@163.com; 1112103001@mail2.gdut.edu.cn; xuou@gdut.edu.cn).
Yuwen Qin is with the Advanced Institute of Photonics Technology, School of Information Engineering, Guangdong University of Technology, Guangzhou, Guangdong 510006, China, with the Guangdong Provincial Key Laboratory of Information Photonics Technology, Guangdong University of Technology, Guangzhou, Guangdong 510006, China, and also with the Synergy Innovation Institute of GDUT, Heyuan, Guangdong 517000, China (e-mail: qinyw@gdut.edu.cn).

1970s, fiber sensors have been developed and promoted in the measurement of different variables such as temperature, torsion, strain, curvature, refractive index, and so on [1]–[4]. As an important physical parameter, curvature can reflect the shape and deformation of the object to be measured. Optic fiber curvature sensors are widely used in non-destructive monitoring civil infrastructure such as bridges and dams, as well as structural health monitoring of ships, automobiles, and spacecrafts. Examples of these curvature sensors are fiber gratings, named: long period gratings (LPGs) [5]–[7], fiber Bragg gratings (FBGs) [8]–[11], tilted fiber Bragg gratings (TFBGs) [12], and chiral fiber gratings (CFGs) [13]. Polymer optical fibers used as curvature sensors have also been investigated [14]. In addition, an off-centered TFBG inscribed in cyclic transparent optical polymer (CYTOP) fiber as a curvature sensor have been studied [15]. Some of the curvature sensors were based on intensity modulation [14]. Fiber optic interferometers have also been adopted in curvature sensing, including multimode interferometers (MMIs) [16], Mach-Zehnder interferometers (MZIs) [17]–[20], Fabry-Pérot interferometers (FPIs) [2]–[3], [21]–[22], anti-resonant (AR) mechanisms [23]–[24], and Sagnac interferometers (SIs) [25].

Among the above curvature sensors, some can be used in two-dimensional (2D) curvature measurement by writing gratings [5]–[12]. Compared with one-dimensional (1D) curvature measurement that can only distinguish positive or negative directions, 2D curvature sensors can tell any curvature direction from $0°$ to $360°$. However, besides high-powered lasers such as UV, femtosecond, and CO_2 lasers, the writing process of gratings is complex, which requires accurate alignment technique. In addition, some of these 2D sensors are created with serial FBGs, and the packaging of these FBGs is also very challenging.

In contrast, fiber optic interferometers have the advantages of simple fabrication, high sensitivity, and versatility [26]. Among various interferometer-based fiber sensors, FPI sensors have been demonstrated in different configurations, for examples, producing an air bubble between two sections of multimode fibers (MMFs) [27] or between single-mode fibers (SMFs) [28], creating the hollow cavities through chemical etching [29], or various laser ablation technologies, containing excimer lasers and femtosecond lasers [26], and utilizing a cold splicing approach based on resin to produce FP cavity [30]–[31]. However, these configurations always depend on challenging manufacturing processes, using dangerous chemicals, or expensive
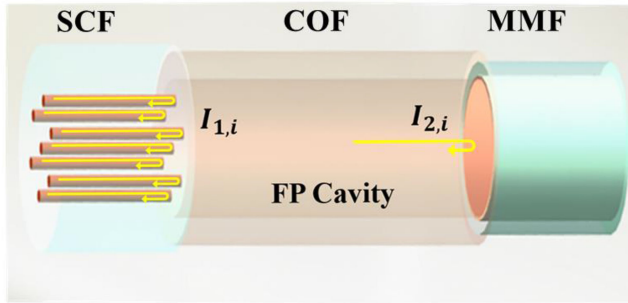
Fig. 1. Schematic diagram of the proposed 2D vector bending sensor based on SCF-COF-MMF.
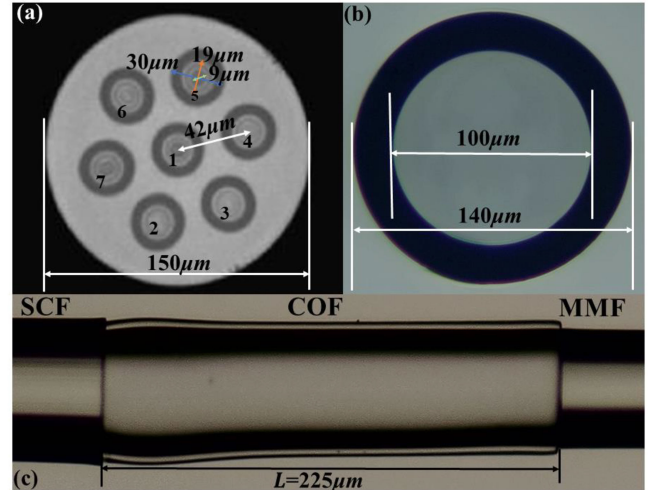

Fig. 2. (a) and (b) Micrograph of the SCF and COF cross sections. (c) The microscope image of this proposed structure.

TABLE I
PARAMETER SETTING OF THE SPLICER

Type	SCF-COF/COF-MMF
Fusion mode	PCF-SMF
Discharge power	Standard-100 bit
Duration time	2 seconds
Discharge time	300 ms
Discharge stop time	500 ms

high-powered lasers. And when the FPI cavity is filled with a resin, it will show high sensitivity to environmental temperature variations, and due to the uneven filling of the resin, the compensation process of temperature effect becomes complicated. Recently, the formation of FPI using a silica capillary optical fiber (COF) has been studied extensively [32]–[34]. They can be used to monitor a variety of parameters, such as, refractive index, strain, and magnetic field. Due to the low thermal-optical coefficient of air in the cavity, these sensors are insensitive to temperature. Moreover, in the process of manufacturing, only cutting and splicing are required, so they have the superiorities of high repeatability, low cost, and simple fabrication. However, the current FPI curvature sensor based on COF can only be used for 1D curvature measurement [35].

In this work, we present and experimentally confirm a temperature-insensitive 2D vector bending sensor based on FPI. The proposed sensor is made through splicing a section of COF between the MMF and trench-assisted seven-core fiber (SCF). The SCF-COF and COF-MMF interfaces act as two FPIs reflectors. The reflection spectra of six outer-core-based FPIs are monitored to measure curvature from different fiber orientation angles. The maximum sensitivity of 200.6 pm/m^{-1} is obtained, which is 3 times higher than that of a FBG vector bending sensor [8]. The orientation angle and curvature magnitude can be reconstructed through the dip wavelength shifts of any two off-diagonal outer-core FPIs. In addition, since the low thermal-optical coefficient of air, the proposed sensor is nearly insensitive to temperature, which has also been verified by temperature experiments.

II. SENSOR FABRICATION AND MEASUREMENT PRINCIPLE

The proposed 2D vector bending sensor is created via splicing a section of COF between the SCF and MMF, as illustrated in Fig. 1. The SCF-COF and COF-MMF interfaces act as two FPIs reflectors. As a result, in the configuration, seven separate FPIs can be produced. Fig. 2(a) reveals a micrograph of the cross section of SCF (YOFC, MC1010-A, China), with a hexagonal arrangement of six outer cores and one central core. The diameter of SCF is 150 μm and between neighboring cores, the distance is 42 μm. As a separate channel, each core possesses three claddings: outer, the secondary, and the inner-field cladding,

with diameters of 30, 19, and 9 μm, respectively. The micrograph of COF (TSP100170) cross section is shown in Fig. 2(b), where the diameters of cladding and air hole respectively are 140 and 100 μm. For the MMF, its core diameter and cladding diameter are 105 and 125 μm, respectively, which is just as one reflector of the FPIs. It is noted that when the fusion splicer (ATOMOWAVE SFS-A60+) is utilized to splice three fibers, manual mode and multiple weak discharges were employed for preventing the air hole collapse in COF [23]. The fusion mode was set as photonic crystal fiber (PCF)-SMF, the discharge power was lower than the standard value of 100 bit. Discharge stop time, discharge time, as well as duration time was 500 ms, 300 ms, and 2 seconds, respectively, that is, a total of three discharges, as shown in Table I. The microscope image of this proposed structure is shown in Fig. 2(c). The COF length is about 225 μm.

On the basis of two-beam interference model, for the output interference light intensity, the expression can be displayed as [36]:

$$I = I_{1,i} + I_{2,i} + 2\sqrt{I_{1,i}I_{2,i}} \cos\varphi, (i = 1, 2, 3, 4, 5, 6, 7) \quad (1)$$

where the $I_{1,i}$ and $I_{2,i}$ represent the light intensities reflected through two interfaces, i denotes the core number of the SCF shown in Fig. 1(a), and φ denotes the difference of optical phase between two beams, which can be expressed with [36]:
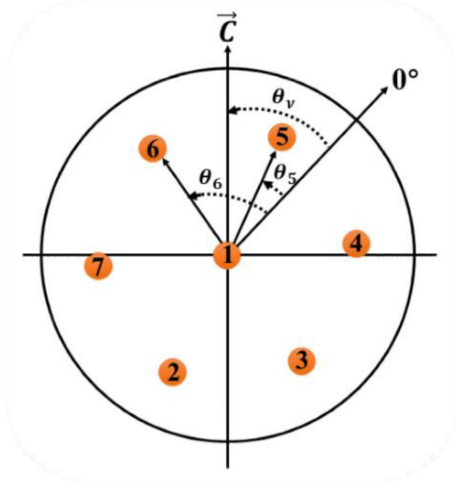
$$\varphi = 4\pi n_0 L_i / \lambda \quad (2)$$

Fig. 3. The diagram of seven-core FPIs bending sensing. The direction of curvature is the convex direction of bending.

Fig. 4. The detected reflection spectra of seven FPIs in presented structure.

in which L_i refers to the ith FPI cavity length, n_0 represents the air refractive index, and λ is the wavelength of light in vacuum. When conforming $\varphi = (2m_i + 1)\pi, (m_i = 0, 1, 2 \ldots)$, for the reflection spectrum on the basis of FPI, the dip wavelength can be described as [36]:

$$\lambda_{m_i} = \frac{4n_0 L_i}{2m_i + 1}, m_i = 0, 1, 2 \ldots \quad (3)$$

where m_i is constant depending on the length of FP cavity, indicating the m_i^{th} resonant wavelength. According to (3), the distance between two adjacent interference wavelengths, that is, the free spectral range (FSR), can be expressed as [33]:

$$FSR = \frac{\lambda_{m_i} \lambda_{(m+1)_i}}{2n_0 L_i} \quad (4)$$

From (3), we can clearly see that in reflection spectrum, the dip wavelength is determined by the cavity length L_i and refractive index n_0, thus, any change in the above two parameters will cause the shifts of dip wavelength. When strain occurs, the corresponding dip wavelength shifts in the FPI reflection spectra can be written as [30]:

$$\frac{\Delta\lambda_{m_i}}{\lambda_{m_i}} = \left(1 + \frac{1}{n_0}\frac{\partial n_0}{\partial \varepsilon_i}\right)\varepsilon_i \quad (5)$$

where $\varepsilon_i = \Delta L_i / L_i$ is the locally-induced strain in i^{th} core.

Fig. 3 reveals the distribution of seven cores. If the presented sensor bends within a specific fiber orientation angle, various strains will be generated in each fiber core. Although some cores are likely to undergo the local compressive strain, others are probably to be elongated locally, determining by the relative angular position between the local bending axis and a specific core. Especially, the strain induced by bending in the core i along the SCF at any point can be displayed as [37]:

$$\varepsilon_i = dC\cos(\theta_i - \theta_\nu) \quad (6)$$

in which d is the distance between outer cores and center core, C is the curvature magnitude, θ_ν can be defined as the
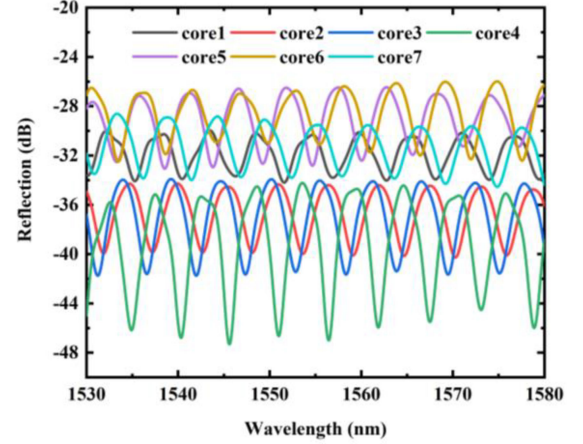
angular offset between $0°$ (optional as reference) and the bending direction of fiber and θ_i denotes the angle between $0°$ and i^{th} core, as reflected in Fig. 2. Replacing (6) into (5), the (5) can be described as:

$$\frac{\Delta\lambda_{m_i}}{\lambda_{m_i}} = \left(\frac{\Delta n_0}{n_0} + d\cos(\theta_i - \theta_v)C\right) \quad (7)$$

Due to the low elasticity-optical coefficient of air, $\Delta n_0/n_0$ can be neglected. Depending on the position of the core i on the fiber and the fiber rotation angle, the dip wavelength will be red- or blue-shifted. In addition, the absolute value of (7) is maximum when θ_i and θ_ν are equal or the difference is π, that is, the direction applied by the curvature is exactly the same as or opposite to the core position. The value of (7) is zero when the core position is orthogonal to the bending direction, that is, the difference between θ_i and θ_ν is $\pi/2$ or $3\pi/2$. However, the center core (core 1) will not be affected by the curvature [8]. The temperature dependence can be expressed by the following formula [30]:

$$\frac{\Delta\lambda_{m_i}}{\lambda_{m_i}} = \left(\frac{1}{n_0}\frac{\partial n_0}{\partial T} + \frac{1}{L_i}\frac{\partial L_i}{\partial T}\right)\Delta T \quad (8)$$

among which, in parentheses, first term represents the normalized thermal-optical coefficient (β), and the second term refers to the normalized thermal-expansion coefficient (α). Since the thermal-optical coefficient in air is low, the presented sensor should have low sensitivity of temperature.

III. TWO-DIMENSIONAL VECTOR BENDING EXPERIMENTS

Before conducting the curvature measurement experiment, the reflection spectra of seven FPIs are measured first as shown in Fig. 4. According to Fig. 4, the loss values of FPIs are different. This may be caused by using ordinary cutting knife that will lead to unevenness end face of SCF, and slight offset will also be introduced in the process of manually alignment in splicing the SCF and COF. Moreover, the measured values of the FSR of the seven-core FPIs near 1550 nm are 5.32, 5.53, 5.49, 5.39, 5.39, 5.63, and 5.53 nm, respectively, which agree well with
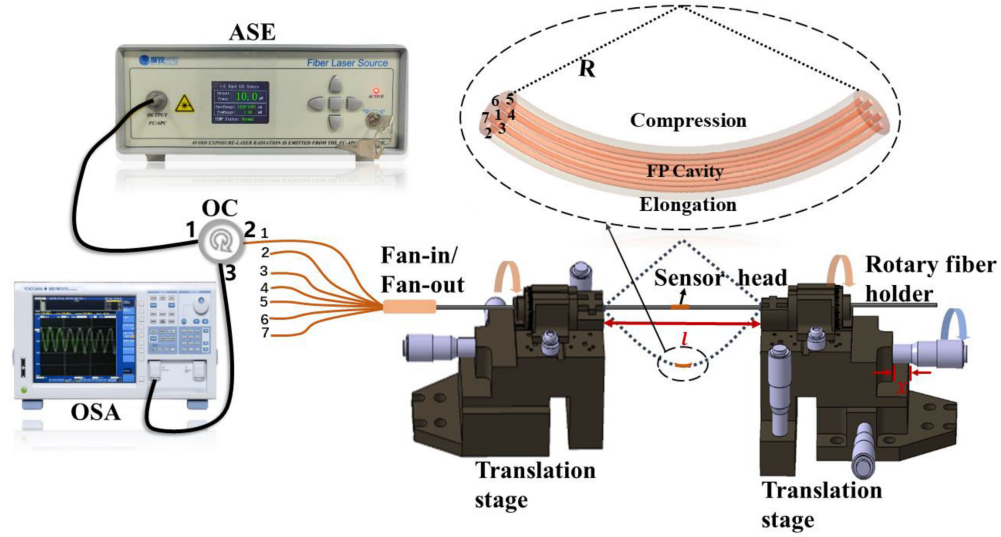
Fig. 5. The experimental setup of 2D vector bending measurement. The inset above shows that FP cavities at different core positions are subjected to different degrees of elongation or compression.

the theoretical calculated value 5.34 nm. It can be observed that between the FSRs in seven FPIs, there exist a small difference. The differences between measured and theoretical FSR values are mainly owing to the COF air hole was slightly squeezed in splicing the COF and SCF, and can be discovered from Fig. 2(c).

The 2D bending response for the presented sensor was studied with the experimental device reflected in Fig. 5. An amplified spontaneous emission with a range of 1508–1583 nm (ASE, MAX-RAY ASE-CL-20-B-T) as a light source into the port 1 of the optical circulator (OC). The port 2 of OC connects with a fan-in/out device, which was spliced with the sensor head mounted on two translation stages by two rotary fiber holders. Finally, an optical spectrum analyzer (OSA, YOKOGAWA AQ6370D) was utilized to monitor reflection spectra with 0.02 nm resolution and linked with port 3 of OC. The stage on the left is fixed, and the other on the right can move controllably inward to raise curvature value. The curvature expression on the basis of the experimental device can be expressed as [17]:

$$C = \frac{1}{R} \cong \sqrt{\frac{24x}{l^3}} \qquad (9)$$

in which R is the radius of bending fiber, x is the displacement of stage on the right, and $l = 17$ cm is the original distance between two stages. The bending characteristics are achieved through moving the stage on the right in steps of 0.8 mm at a time, allowing the application of curvature, which reaches 5.93 m^{-1}. For each of the curvature step, the reflection spectra were gathered. Via rotating two rotary optical fiber holders at the same time, the bending characterization of each optical fiber orientation angle was performed in steps of 30° between 0° and 360°. In order to prevent the sensor head twisting during the experimental measurements, we put the sensor head into a segment of capillary to increase its weight. Experiments have verified the direction dependence of the presented sensor.
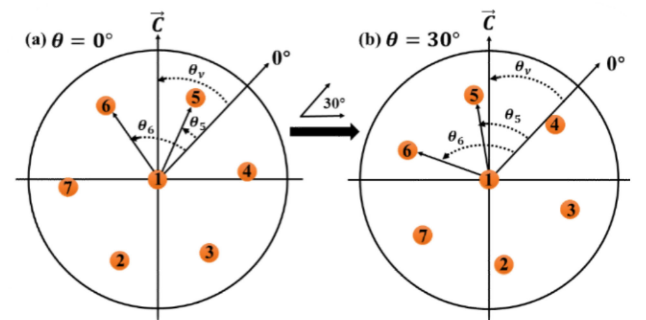

Fig. 6. Schematic diagram of SCF cross-sections under a vector curvature (a) at the initial position ($\theta = 0°$) and (b) Rotating by 30° ($\theta = 30°$).

As shown in Fig. 6(a), θ is defined as the fiber orientation angle, and $\theta = 0°$ is the initial orientation angle of the sensor head. Keeping the fiber orientation angle, the dip wavelength shifts of six outer cores were recorded with applied curvatures, which are shown in Fig. 7(a). We can see from Fig. 7(a) that the FPIs corresponding to cores 2, 3, and 7 are in the compression, while which of cores 4, 5, and 6 are in tension, respectively displaying negative or positive dip wavelength shifts. In the consideration of SCF is completely symmetrical and cores 2 and 5 are 42 μm away from central core, their sensitivities should be equal. The values acquired in the experiment respectively are −157.3 and 155.8 pm/m^{-1} for cores 2 and 5, with similar magnitudes. For the cores along other diagonal lines, including cores 3 and 6 as well as cores 4 and 7, the sensitivities were −126.6, 132.8, 16.4, and −29.9 pm/m^{-1}, respectively. In summary, the cores along the same diagonal lines have the similar sensitivities in magnitude, which are lower than that obtained for cores 2 and 5. According to the (7), the core with larger θ_i will have smaller wavelength shifts, proving that the experimental responses are in agreement with theoretical analysis above.
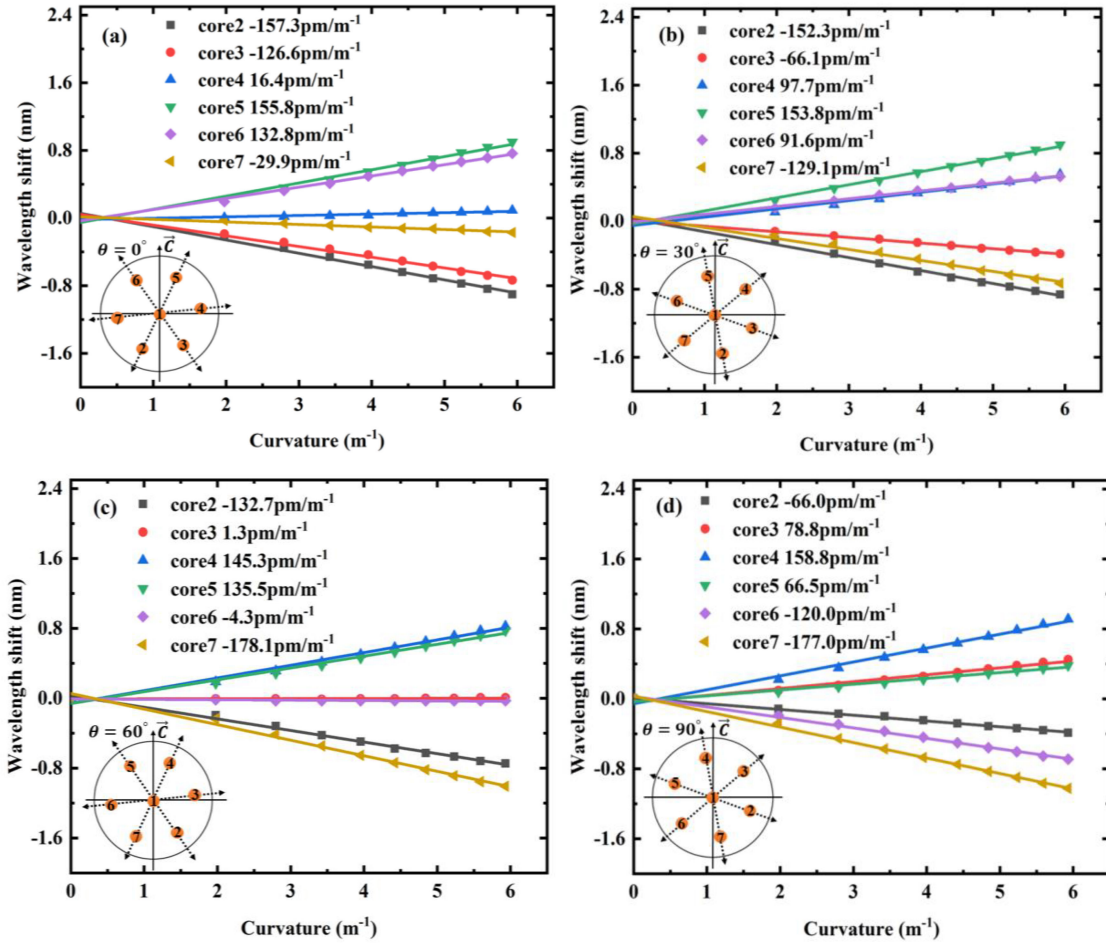
Fig. 7. Linear fitting curves of dip wavelength shifts against curvature variations for the six outer-core FPIs, regarding the fiber orientation angles of (a) 0°, (b) 30°, (c) 60°, and (d) 90°. The sensitivities of each FPI are also presented.

Then rotating the sensor head by 30° (θ) using the rotary fiber holders, the SCF cross section reflected in Fig. 6(b) can be obtained. The dip wavelength shifts of six outer cores under the same curvature were recorded and shown in Fig. 7(b). The results in Fig. 7(b) show that when θ, the fiber orientation angle varies, for each core, the response also changes with the strain of radial position of each core (reflected in (7)). When $\theta = 60°$ shown in Fig. 7(c), we can see that the SCF core-distribution is the same as in Fig. 6(a), but the location of the original core is different. As a result, cores 7 and 4 should possess similar curvature sensitivity amplitudes. In accordance with the symmetrical arrangement of the outer core, their sensitivities shall be similar to that of cores 2 and 5 ($\theta = 0°$), respectively. And the sensitivities of other cores should be lower in magnitude than cores 4 and 7. From the experimental results, as shown in Fig. 7(c), cores 4 and 7 were 145.3 and -178.1 pm/m^{-1}, respectively, which were slightly different between the two cores and from cores 5 and 2 ($\theta = 0°$). This small difference may be caused by irregularly cutting fiber ends and slight deformation of COF air hole when splicing COF and SCF during sensor manufacturing. In addition, the sensitivities of cores 2, 3, 5, and 6 shown in Fig. 6(c) were -132.7, 1.3, 135.5, and -4.3 pm/m^{-1}, respectively, which had

a lower magnitude in comparison with that in cores 4 and 7. Therefore, the experimental results were consistent with the above analysis. Similarly, when $\theta = 90°$, as shown in Fig. 7(d), the SCF position was the same with Fig. 7(b), but the positions of ith core were different. Therefore, the curvature sensitivity of each core in Fig. 7(d) should be the same as the curvature sensitivity of the corresponding core located in the same angular position in Fig. 7(b). And the data represented in the Fig. 7(b) and 7(d) showed that our analysis were consistent with the experimental results.

Accordingly, in order to clearly see the curvature characteristics of each core at different fiber rotation angles, the outcomes of two FPIs along the identical diagonal (cores 2 and 5) are displayed in the Fig. 8(a) and 8(b). Linear fittings are applied to the dip wavelength shifts at given fiber orientation angles θ, and the slope denotes the curvature sensitivity. The outcomes suggest that for the FPI based on two outer cores along an identical diagonal line, curvature sensitivities possess an opposite dip wavelength shifts and similar amplitude at any orientation angle θ. For a fixed core, with different orientation angles θ, the dip wavelength shifts are different (red- or blue- shifted), this is mainly due to the change of the core position (θ_i), which will
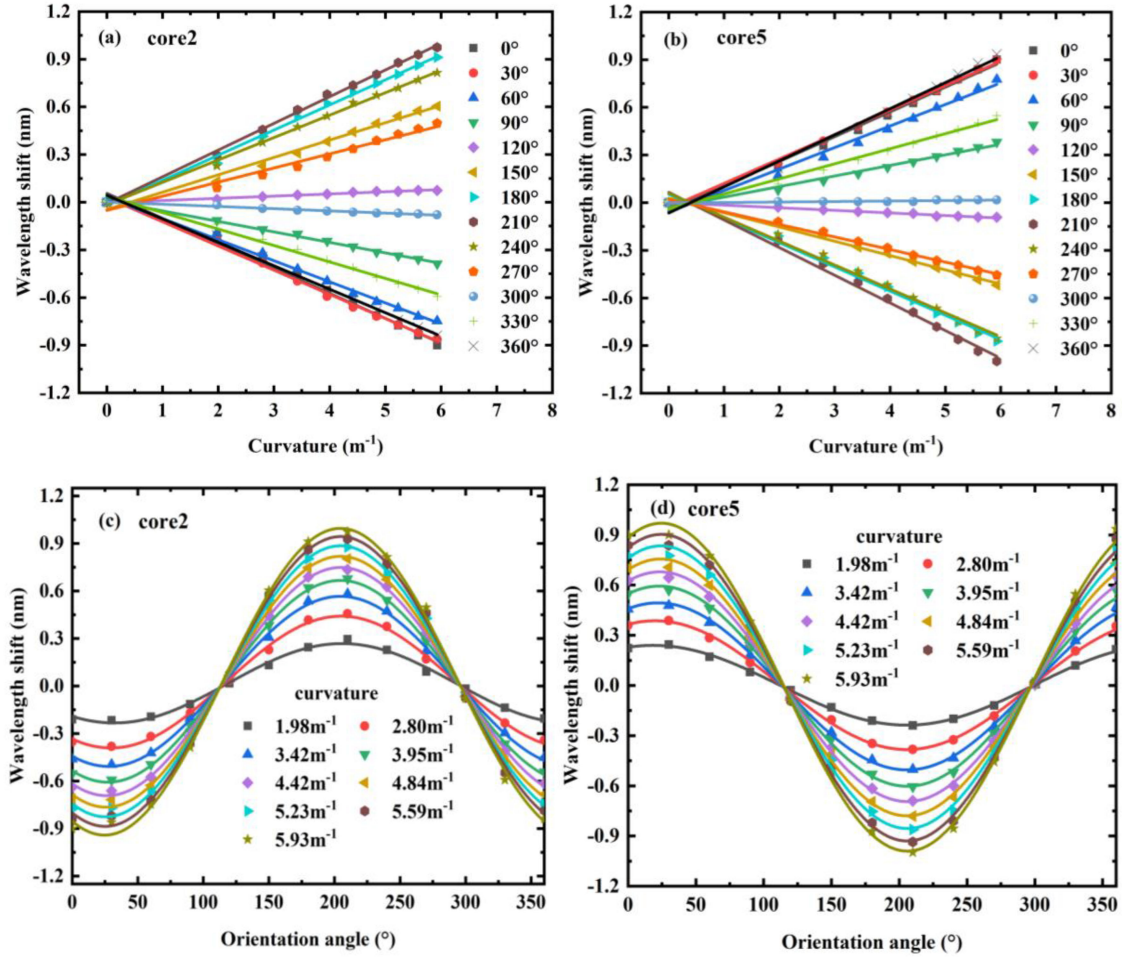
Fig. 8. Shifts of dip wavelength relative to curvature measured for various orientations: (a) Core 2 and (b) Core 5. Also reflected are the shifts of dip wavelength for (c) Core 2 and (d) Core 5, drawn as a function of orientation angle.

lead to the change of dip wavelength shifts in (7). Fig. 8(c) and 8(d) reveal that the dip wavelength of cores 2 and 5 changes as the orientation angles θ increases. All the changes of dip wavelength under a specific curvature exhibit good consistency with the sinusoidal behavior [8]. Fig. 9 plots the data of cores 2, 3, and 4 in polar coordinates, and clearly reflects the symmetrical "8"-shaped distributions, in which it is easy to see the angle difference of 60°. The directions of the maximum curvature sensitivities are 85°, 145°, and 205° for cores 4, 3, and 2, respectively. Therefore, the original 0° can be acquired through the calculation on the basis of the determined responses [39].

With an aim of understanding the maximum curvature sensitivity S_i, the sinusoidal curves were fitted into the data of experiment in Fig. 10 to obtain the following values: 173.8, 167.7, −172.8, −173.0, −200.6, and −181.7 pm/m^{-1}, for cores 2, 3, 4, 5, 6, and 7, respectively. It is 3 times higher than the one reported (59.47 pm/m^{-1}) for FBGs written on a similar SCF [8], and 2 times higher than the one reported (81.5 pm/m^{-1}) for 1D bending vector sensor on the basis of the similar air cavity FPI [35]. The curvature sensitivities of each outer-core FPI are slightly different, due to errors produced during fiber cleaving and splicing. Additionally, we can clearly see that between cores

2 and 4, the change of angle is 120°, which is in accordance with the angle separation of 120° in SCF. And the angle change for cores 2 and 3 is in accordance with the angle separation of 60° in the SCF.

In addition, increasing and decreasing curvatures experiments were performed to verify the proposed sensor is repeatable. Fig. 11 shows that linear fit curves of the dip wavelength shifts of the six outer cores with increasing and decreasing curvatures at a fixed orientation angle. Experimental results show that the proposed sensor has good curvature repeatability.

Besides above experiments, we have also measured the temperature effect of the seven independent FPIs, ranging from 30 °C to 100 °C. The dip wavelength variations of seven FPIs with increasing temperatures are displayed in Fig. 12. For seven FPIs, their temperature sensitivities are 0.40, 0.67, 0.39, 0.57, 0.29, 0.52, and 0.20 pm/°C, respectively. It can be seen that there are some differences between the temperature sensitivities of the seven FPIs. This is due to the uneven cutting end face of the SCF during the manufacturing process, resulting in some slight differences between the cavity lengths of the seven FPIs. However, this does not affect the measurement of 2D vector bending. In comparison with 200.6 pm/m^{-1} of the maximum
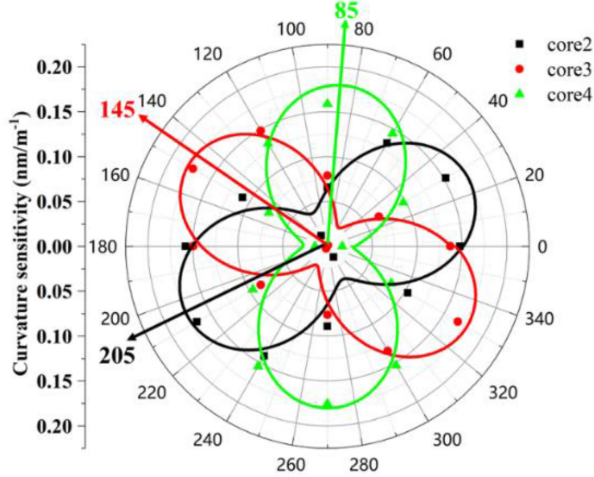
Fig. 9. Orientation dependence of FPIs sensitivities in core 2, core 3, and core 4 in polar coordinates.
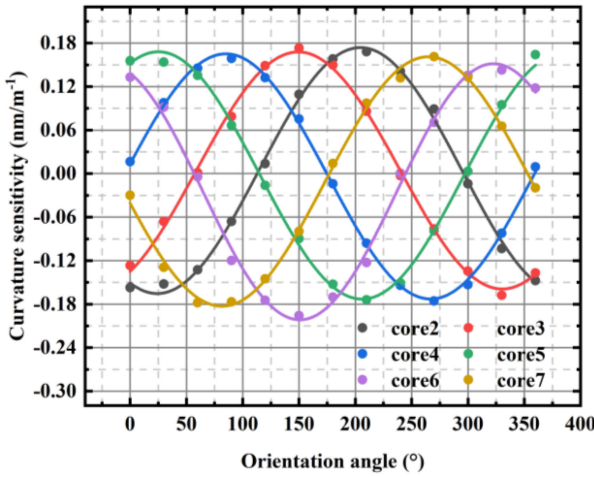

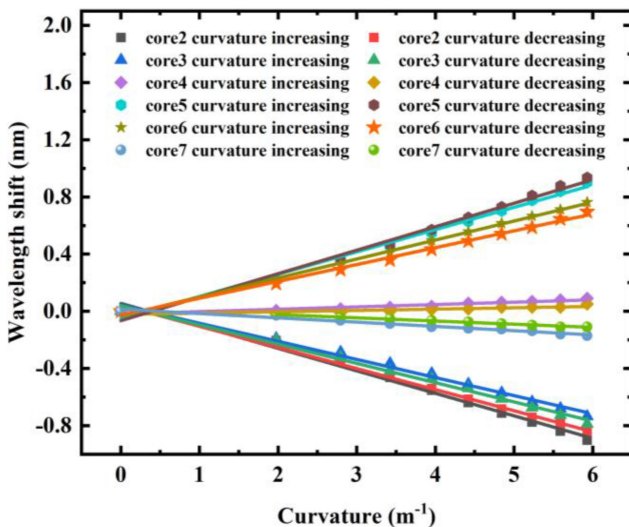Fig. 10. Curvature sensitivities as function of the orientation angle.

Fig. 11. Linearly fitted curves of dip wavelength shifts against curvatures.
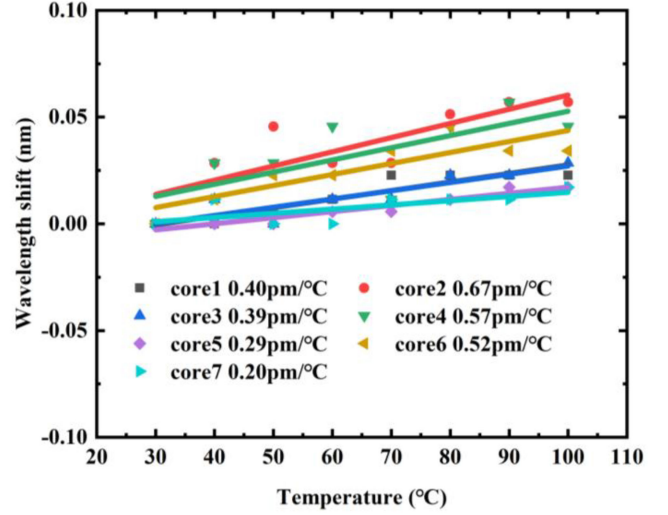

Fig. 12. Dip wavelength shifts as the function of seven-core FPIs temperature.

curvature sensitivity, the cross sensitivity between temperature and curvature is calculated as temperature sensitivity divided by curvature sensitivity [40], which is only 0.0009 m^{-1}/°C.

IV. CURVATURE MAGNITUDE AND ORIENTATION ANGLE RECONSTRUCTION

The correlation between orientation angle and curvature sensitivity for each outer-core FPI can be fitted with the sinusoidal function, as displayed in Fig. 10. The fitting equation is described as [6]:

$$S_i = y_i + A_i \sin(\theta - \theta_i) \tag{10}$$

where S_i represents the curvature sensitivity in direction θ, and y_i, A_i, and θ_i are constants which acquired from Fig. 10.

Any two functions of off-diagonal outer cores from Fig. 10, such as cores 2 and 4, can form a matrix as follows [6]:

$$\begin{bmatrix} \Delta\lambda_2 \\ \Delta\lambda_4 \end{bmatrix} = C \cdot \begin{bmatrix} y_2 + A_2 \sin(\theta - \theta_2) \\ y_4 + A_4 \sin(\theta - \theta_4) \end{bmatrix} \tag{11}$$

where $\Delta\lambda_2$ and $\Delta\lambda_4$ are the dip wavelength shifts of cores 2 and 4 FPIs, respectively. C represents the curvature magnitude of presented sensor in direction θ. $\Delta\lambda_2$ and $\Delta\lambda_4$ can be obtained by curvature measuring. Therefore, the orientation angle θ and curvature magnitude C can be acquired with (11). A set of sampling data was applied to detect the reconstruction property for seven-core FPI. For a specific set of conditions ($\theta = 30°$ and $C = 4.8$ m^{-1}), for six outer-core FPIs, their detected dip wavelength shifts ($\Delta\lambda_i$) are -0.72, -0.32, 0.43, 0.71, 0.44 and -0.58 nm, respectively. The curvature magnitude C and orientation angle θ can be reconstructed by (11). There are 12 different combinations in total, as shown in Table II. The average reconstruction result (4.4 m^{-1}, $29°$) of 12 different combinations is very close to the actual value (4.8 m^{-1}, $30°$). The average relative error is about 6.2% for reconstructed curvature magnitude and about 3.3% for the orientation angle θ, which are

TABLE II
THE CURVATURE (4.8 M^{-1}, 30°) RECONSTRUCTED FOR 12 VARIOUS
COMBINATIONS

Reconstructed combination	C=4.8m^{-1}	θ=30°
(core2, core3)	4.4	30
(core2, core4)	4.4	31
(core2, core6)	4.4	22
(core2, core7)	4.5	34
(core3, core4)	4.5	31
(core3, core5)	4.2	29
(core3, core7)	4.7	32
(core4, core5)	4.3	32
(core4, core6)	4.9	27
(core5, core6)	4.3	21
(core5, core7)	4.3	36
(core6, core7)	4.3	23
Average	4.4	29

lower than the errors in prior studies (about 8%) [37]–[38], revealing excellent reliability and high accuracy of the method for reconstructing the orientation angle and curvature magnitude.

In summary, structures similar to the proposed sensor have not been studied before. Although its sensing principle is similar to [30], due to the low thermo-optical coefficient of air, the problem of temperature compensation can be ignored. At the same time, only cutting and welding techniques are required in manufacturing, so the cost is low. Compared with the grating writing techniques [8], [15], expensive lasers and precise alignment techniques are not required. In addition, compared with the fused polymer optical fiber [14], the used optical fiber can be easily obtained and does not need to be damaged by the fiber fusing. Curvature sensitivity of the proposed sensor is high and the relative errors of curvature magnitude and orientation angle reconstruction are small. It has important research prospects in 2D vector bending measurement.

V. CONCLUSION

We have presented and experimentally confirmed a temperature-insensitive 2D vector bending sensor in a SCF. In all 360° directions, for the six outer-core FPIs, their bending responses were studied at a step of 30°. The curvature sensitivities of six outer-core FPIs have strong angular dependences, and the maximum sensitivity is 200.6 pm/m^{-1}. It is about 3 times higher than the one (59.47 pm/m^{-1}) based on FBGs written on a similar SCF [8], and 2 times higher than the one (81.5 pm/m^{-1}) reported for 1D bending vector sensor on the basis of similar air cavity FPI [35]. Moreover, the temperature effect influence on the proposed sensor can be nearly ignored. The curvature magnitude and orientation angle could be reconstructed utilizing the obtained outer-core FPI dip wavelength shifts and fitted sine functions of curvature sensitivity against orientation angle. There are 12 different combinations which can be used for reconstructing the curvature magnitude C and orientation angle θ. For a given set

of orientation angle and curvature magnitude (30°, 4.8 m^{-1}), the reconstructed average value of 12 various combinations (29°, 4.4 m^{-1}) has a relative error of 6.2% for curvature magnitude C and 3.3% for the orientation angle θ. The temperature-insensitive 2D vector bending sensor has significant potential in fiber shape sensing applications.

REFERENCES

[1] C. Yin, R. Wang, S. Jing, and L. Gao, "A stretchable and highly sensitive graphene-based fiber for sensing tensile strain, bending, and torsion," *Adv. Mater.*, vol. 27, no. 45, pp. 7365–7371, Dec. 2015.

[2] M. Cano-Contreras et al., "All-fiber curvature sensor based on an abrupt tapered fiber and a Fabry–Pérot interferometer," *IEEE Photon. Technol. Lett.*, vol. 26, no. 22, pp. 2213–2216, Nov. 2014.

[3] O. Y. Yang, J. Kong, Y. M. Xu, A. Zhou, and L. B. Yuan, "Simultaneous measurement of temperature and bend by using an eccentric core fiber Bragg grating cascaded with a Fabry-Perot cavity," in *Proc. 25th Int. Conf. Opt. Fibre Sensors*, Art. no. 1032375, doi: 10.1117/12.2264894.

[4] C. R. Liao, T. Y. Hu, and D. N. Wang, "Optical fiber Fabry-Perot interferometer cavity fabricated by femtosecond laser micromachining and fusion splicing for refractive index sensing," *Opt. Exp.*, vol. 20, no. 20, pp. 22813–22818, Sep. 2012.

[5] P. C. Geng et al., "Two-dimensional bending vector sensing based on spatial cascaded orthogonal long period fiber," *Opt. Exp.*, vol. 20, no. 27, pp. 28557–28562, Dec. 2012.

[6] S. Wang et al., "Two-dimensional microbend sensor based on long-period fiber gratings in an isosceles triangle arrangement three-core fiber," *Opt. Lett.*, vol. 42, no. 23, pp. 4938–4941, Dec. 2017.

[7] D. Barrera, J. Madrigal, and S. Sales, "Long period gratings in multicore optical fibers for directional curvature sensor implementation," *J. Lightw. Technol.*, vol. 36, no. 4, pp. 1063–1068, Feb. 2018.

[8] M. X. Hou et al., "Two-dimensional vector bending sensor based on seven-core fiber Bragg gratings," *Opt. Exp.*, vol. 26, no. 18, pp. 23770–23781, Sep. 2018.

[9] K. M. Yang et al., "Femtosecond laser inscription of fiber Bragg grating in twin-core few-mode fiber for directional bend sensing," *J. Lightw. Technol.*, vol. 35, no. 21, pp. 4670–4676, Nov. 2017.

[10] H. L. Zhang et al., "Fiber Bragg gratings in heterogeneous multicore fiber for directional bending sensing," *J. Opt.*, vol. 18, no. 8, Aug. 2016, Art. no. 085705, doi: 10.1088/2040-8978/18/8/085705.

[11] W. J. Bao, Q. Z. Rong, F. Y. Chen, and X. G. Qiao, "All-fiber 3D vector displacement (bending) sensor based on an eccentric FBG," *Opt. Exp.*, vol. 26, no. 7, pp. 8619–8627, Apr. 2018.

[12] D. Y. Feng, W. J. Zhou, X. G. Qiao, and J. Albert, "Compact optical fiber 3D shape sensor based on a pair of orthogonal tilted fiber Bragg gratings," *Sci. Rep.*, vol. 5, no. 1, pp. 1–7, Nov. 2015. doi: 10.1038/srep17415.

[13] R. D. Wang, Z. Y. Ren, X. D. Kong, D. P. Kong, B. W. Hu, and Z. Q. He, "Mechanical rotation and bending sensing by chiral long-period grating based on an axis-offset rotating optical fiber," *Appl. Phys. Exp.*, vol. 12, no. 7, Jul. 2019, Art. no. 072013, doi: 10.7567/1882-0786/ab2a20.

[14] A. Leal-Junior et al., "Design and characterization of a curvature sensor using fused polymer optical fibers," *Opt. Lett.*, vol. 43, no. 11, pp. 2539–2542, Jun. 2018.

[15] A. Leal-Junior et al., "Temperature-insensitive curvature sensor with plane-by-plane inscription of off-center tilted bragg gratings in CYTOP fibers," *IEEE Sens. J.*, vol. 22, no. 12, pp. 11725–11731, Jun. 2022.

[16] Q. Wu et al., "Singlemode-multimode-singlemode fiber structures for sensing applications—A review," *IEEE Sens. J.*, vol. 21, no. 11, pp. 12734–12751, Jun. 2020.

[17] W. H. Yuan, Q. C. Zhao, L. D. Li, Y. Wang, and C. Y. Yu, "Simultaneous measurement of temperature and curvature using ring-core fiber-based Mach-Zehnder interferometer," *Opt. Exp.*, vol. 29, no. 12, pp. 17915–17925, Jun. 2021.

[18] C. Li et al., "All-fiber multipath Mach–Zehnder interferometer based on a four-core fiber for sensing applications," *Sens. Actuator A Phys.*, vol. 248, pp. 148–154, Sep. 2016.

[19] C. Y. Guan, X. Zhong, G. P. Mao, T. T. Yuan, J. Yang, and L. B. Yuan, "In-line Mach–Zehnder interferometric sensor based on a linear five-core fiber," *IEEE Photon. Technol. Lett.*, vol. 27, no. 6, pp. 635–638, Mar. 2015.

[20] J. H. Zhang et al., "Bending vector sensor based on Mach-Zehnder interferometer using S type fibre taper and lateral-offset," *J. Mod. Opt.*, vol. 63, no. 21, pp. 2146–2150, 2016.

[21] C. S. Monteiro et al., "Fiber Fabry-Perot interferometer for curvature sensing," *Photonic Sens.*, vol. 6, no. 4, pp. 339–344, Dec. 2016.

[22] F. X. Zhu et al., "Fabry-Perot vector curvature sensor based on cavity length demodulation," *Opt. Fiber Technol.*, vol. 60, Dec. 2020, Art. no. 102382, doi: 10.1016/j.yofte.2020.102382.

[23] B. B. Qi et al., "A compact fiber cascaded structure incorporating hollow core fiber with large inner diameter for simultaneous measurement of curvature and temperature," *IEEE Photon. J.*, vol. 14, no. 1, Feb. 2022. Art no. 6812208, doi: 10.1109/JPHOT.2022.3144506.

[24] S. Wang et al., "An inline fiber curvature sensor based on anti-resonant reflecting guidance in silica tube," *Opt. Laser Technol.*, vol. 111, pp. 407–410, Apr. 2019.

[25] H. P. Gong, H. F. Song, S. L. Zhang, Y. X. Jin, and X. Y. Dong, "Curvature sensor based on hollow-core photonic crystal fiber sagnac interferometer," *IEEE Sens. J.*, vol. 14, no. 3, pp. 777–780, Mar. 2014.

[26] K. Menghrajani, "Fibre-optic Fabry–Perot sensors: An introduction," *Contemporary Phys.*, vol. 59, no. 4, pp. 402–403, 2018, doi: 10.1080/00107514.2018.1501434.

[27] S. Novais, S. O. Silva, and O. Frazo, "Curvature detection in a medical needle using a Fabry-Perot cavity as an intensity sensor," *Measurement*, vol. 151, Feb. 2020, Art. no. 107160, doi: 10.1016/j.measurement.2019.107160.

[28] S. Liu et al., "High-sensitivity strain sensor based on in-fiber improved Fabry–Perot interferometer," *Opt. Lett.*, vol. 39, no. 7, pp. 2121–2124, Apr. 2014.

[29] P. H. Zhang, L. Zhang, Z. Y. Wang, X. Y. Zhang, and Z. D. Shang, "Sapphire derived fiber based Fabry-Perot interferometer with an etched micro air cavity for strain measurement at high temperatures," *Opt. Exp.*, vol. 27, no. 19, pp. 27112–27123, Sep. 2019.

[30] R. Oliveira, M. Cardoso, and A. M. Rocha, "Two-dimensional vector bending sensor based on Fabry-Pérot cavities in a multicore fiber," *Opt. Exp.*, vol. 30, no. 2, pp. 2230–2246, Jan. 2022.

[31] A. G. Leal Jr. et al., "Fabry-Perot curvature sensor with cavities based on UV-curable resins: Design, analysis and data integration approach," *IEEE Sens. J.*, vol. 19, no. 21, pp. 9798–9805, Nov. 2019.

[32] C. E. Dominguez-Flores, D. Monzon-Hernandez, V. P. Minkovich, J. A. Rayas, and D. Lopez-Cortes, "In-fiber capillary-based micro Fabry-Perot interferometer strain sensor," *IEEE Sens. J.*, vol. 20, no. 3, pp. 1343–1348, Feb. 2020.

[33] Y. Ouyang, X. Xu, Y. Zhao, A. Zhou, and L. Yuan, "Temperature compensated refractometer based on parallel fiber Fabry–Pérot interferometers," *IEEE Photon. Technol. Lett.*, vol. 30, no. 13, pp. 1262–1265, Jul. 2018.

[34] G. K. B. Costa et al., "In-fiber Fabry-Perot interferometer for strain and magnetic field sensing," *Opt. Exp.*, vol. 24, no. 13, pp. 14690–14696, Jun. 2016.

[35] J. Kong, A. Zhou, and L. B. Yuan, "Temperature insensitive one-dimensional bending vector sensor based on eccentric-core fiber and air cavity Fabry-Perot interferometer," *J. Opt.*, vol. 19, no. 4, Apr. 2017, Art. no. 045705, doi: 10.1088/2040-8986/aa535b.

[36] Y. Yu et al., "Coexistence of transmission mechanisms for independent multi-parameter sensing in a silica capillary-based cascaded structure," *Opt. Exp.*, vol. 29, no. 17, pp. 27938–27950, Aug. 2021.

[37] Z. Y. Zhao, M. A. Soto, M. Tang, and L. Thevenaz, "Distributed shape sensing using Brillouin scattering in multi-core fibers," *Opt. Exp.*, vol. 24, no. 22, pp. 25211–25223, Oct. 2016.

[38] D. Zheng, J. Madrigal, H. L. Chen, D. Barrera, and S. Sales, "Multicore fiber-Bragg-grating-based directional curvature sensor interrogated by a broadband source with a sinusoidal spectrum," *Opt. Lett.*, vol. 42, no. 18, pp. 3710–3713, Sep. 2017.

[39] R. Zhou, F. Y. Chen, S. S. Li, R. H. Wang, and X. G. Qiao, "Three-dimensional vector accelerometer using a multicore fiber inscribed with three FBGs," *J. Lightw. Technol.*, vol. 39, no. 10, pp. 3244–3250, May. 2021.

[40] B. Wang et al., "Mach–Zehnder interferometer based on interference of selective high-order core modes," *IEEE Photon. Technol. Lett.*, vol. 28, no. 1, pp. 71–74, Jan. 2016.